Progress In Electromagnetics Research, PIER 44, 287–308, 2004

ELECTROMAGNETIC ANALYSIS OF A NON-INVASIVE 3D PASSIVE MICROWAVE IMAGING SYSTEM

I. S. Karanasiou, N. K. Uzunoglu, and A. Garetsos

Microwave and Fiber Optics Laboratory
Department of Electrical and Computer Engineering
National Technical University of Athens
Greece

Abstract—A technique based on the Green's function theory is used in the present research in order to study theoretically the focusing properties of a constructed 3D non-invasive microwave imaging system, consisting of an ellipsoidal conductive cavity and a radiometric receiver. A double layered spherical human head model is placed on one focal point of the elliptical reflector, while the receiving antenna is placed on the other focus. Making use of the reciprocity theorem, the equivalent problem of the coupling between an elementary dipole and the double layered lossy dielectric human spherical model is solved. Numerical results concerning the electric field distribution inside the head model and in the rest of the cavity, at two operating frequencies (1.5 GHz and 3.5 GHz), are presented and compared to the results of an electromagnetic simulator. Finally, phantom experimental results validate the proof of concept and determine the temperature and spatial attributes of the system.

Appendix A.

References

1. INTRODUCTION

During the past few years efforts have been made by several research groups to implement intracranial applications of microwave radiometry [1–3], due to the fact that microwaves at the frequency region of 1–5 GHz provide sufficient penetration depth into the human body and satisfactory directivity. Total power radiometric systems developed over the years for medical and other applications, are discussed in numerous papers [4–6], mainly consisting of radiometric systems with contacting antennas. Edrich and Hardee developed a different kind of system in 1974 [7], suggesting the use of a horn antenna with a dielectric lens attached to the input of a total power receiver at 45 GHz for the purpose of scanning an object. The infrared region though is limited in its usefulness because living tissue readily absorbs it and hence, only signals originating from the surface can be detected [8].

In the present paper, an innovative approach is introduced; a total power receiver and relevant non-contacting antenna operating at 3.5 GHz are used and the radiation emitted by the human body is focused by an ellipsoidal reflector into the omnidirectional receiving antenna connected to the sensitive total power radiometer. The purpose of designing and constructing such a system was to potentially perform imaging within the human skull for brain intracranial diagnostic applications. The ellipsoidal conductive wall cavity is essentially used as a three dimensional analog beamformer, exploiting the fact that every ray originating from one focus will merge on the other focus with the same path length. Therefore, given that the human head is placed at one focal point inside the ellipsoidal reflector and that the receiving antenna is placed at the other focal point, convergence of the radiated electromagnetic energy from the human brain in the microwave frequency regime, is achieved.

The theoretical analysis of chaotic radiation emerging from material objects, under the condition of thermodynamic equilibrium of matter with radiation, has been explained by Max Planck in the beginning of the 20th century, when he set the foundations of Quantum Theory [9]. This theory was based on the concept of the ideal black body and was formed to explain experimental observations of the chaotic radiation. Hence, when a lossy media is placed inside a cavity with perfect conducting walls to provide an absolute isolation from the surrounding space, the chaotic currents inside the lossy media

generated by the radiation sources, cause an electric field distribution inside the conductor wall cavity.

In the framework of the present research, in order to model the field distribution inside an ellipsoidal conductive cavity in the presence of a human head and especially the focusing properties of the elliptical reflector, a semi-analytical technique is presented, based on the use of the dyadic's Green's function theory. By imposing the appropriate boundary conditions at a finite number of points on the physical surfaces of the scattering objects and on the perfect conductor wall cavity, the unknown coefficients of the dyadic Green's function are determined and therefore, the electric field is calculated at any arbitrary point of the above configuration.

The present paper provides details on the theoretical analysis and mathematical formulation of the problem and it discusses also, the experimental results using phantoms as testing objects of an experimental system prototype.

2. MATHEMATICAL FORMULATION — DYADIC GREEN'S FUNCTION OF THE LAYERED SPHERE

The geometry of the problem is depicted in Fig. 1. The head is modeled by a double-layered sphere with radii a_1 and a_2. The two layers are used to simulate different biological media; bone and brain (gray matter) tissues. The center of the head is placed on one of the two focal points regions of a conductive wall ellipsoidal cavity. The ellipsoidal by revolution that confines the spherical model of the human head, is defined by the following equation:

$$\frac{x^2+y^2}{a^2}+\frac{z^2}{b^2}=1 \tag{1}$$

The interior of the ellipsoidal is filled with air having wavenumber $k_0 = \omega\sqrt{\varepsilon_0\mu_0}$, where ω is the radian frequency, ε_0 and μ_0 are the free-space permittivity and permeability, respectively. The system is excited by an elementary dipole, which is placed on the other focal point of the ellipsoidal. The problem can be solved with all antenna orientations by considering the axis of the dipole parallel to the x-axis, y-axis and z-axis of the coordinate system for each one of the three solutions. The time dependence of the field quantities is assumed to be $e^{i\omega t}$ and is suppressed throughout the analysis. In order to solve this boundary value problem, a Green's function technique is adopted.

According to the Reciprocity theorem, a response of a system to a source is unchanged when source and measurer are interchanged. Hence, instead of placing the source in the head model, the response

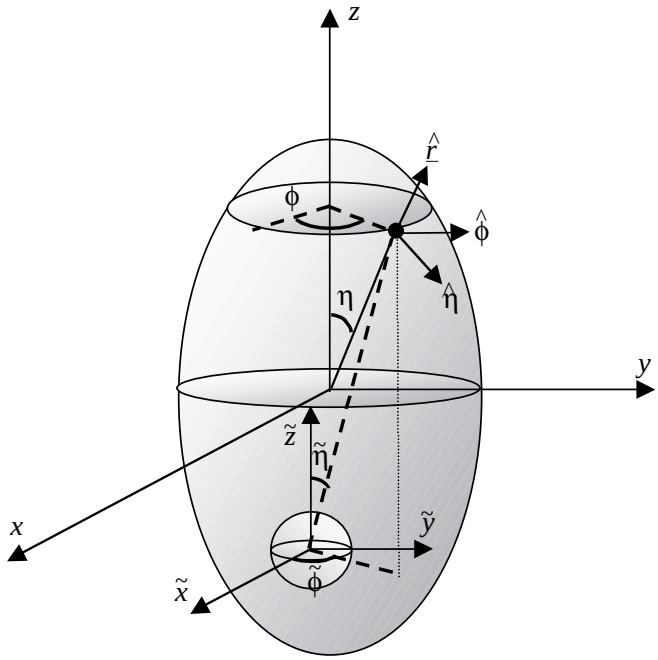

Figure 1. The geometry of the problem.

of the double-layered sphere, placed on one focal point of an ellipsoidal cavity, to the excitation generated by an elementary dipole of unit dipole moment, positioned on the other focus, is calculated. To determine the Green's function of the lossy dielectric sphere, a method based on the superposition principle is employed [10]. Therefore, the unknown dyadic Green's function in each region $i = 1,\ 2,\ 3$ of space is properly expanded to an infinite sum of spherical waves satisfying the appropriate vector wave equation.

In the following analysis two Cartesian coordinate systems are used: one defined as central, with origin the point of section of the major and minor axes of the ellipsoidal and the other defined as local, with origin the center of the sphere, as shown in Fig. 1. The unit vectors of each coordinate system are denoted as $\hat{x},\ \hat{y},\ \hat{z}$ and $\hat{\tilde{x}},\ \hat{\tilde{y}},\ \hat{\tilde{z}}$ for the central and local coordinate system respectively. Given the displacement of the head from the focal point $\delta x,\ \delta y,\ \delta z$ in central coordinates, the transformation expression between the coordinates of the two systems is defined by

$$\tilde{x} = x - \delta x, \qquad \tilde{y} = y - \delta y, \qquad \tilde{z} = z - \delta z \tag{2}$$

By virtue of the spherical symmetry of the problem, the relevant central and local spherical coordinates are used, with unit vectors $\hat{r},\ \hat{n},\ \hat{\varphi}$ and $\hat{\tilde{r}},\ \hat{\tilde{n}},\ \hat{\tilde{\varphi}}$ respectively.

Considering the finiteness of the field at $\tilde{r} = 0$, the following expressions describe the electric-type Green's function inside the layered sphere:

$$\overline{\underline{G}}_1(\underline{\tilde{r}}, \underline{\tilde{r}}') = \sum_{n=1}^{\infty}\sum_{m=-n}^{n}\left[\underline{m}_{mn}^{(1)}(\underline{\tilde{r}}, k_1)\underline{a}_{mn}(\underline{\tilde{r}}') + \underline{n}_{mn}^{(1)}(\underline{\tilde{r}}, k_1)\underline{a}'_{mn}(\underline{\tilde{r}}')\right], \quad \tilde{r} \le a_1 \tag{3}$$

$$\begin{aligned}\overline{\underline{G}}_2(\underline{\tilde{r}}, \underline{\tilde{r}}') = \sum_{n=1}^{\infty}\sum_{m=-n}^{n}\Big[&\left(\underline{m}_{mn}^{(1)}(\underline{\tilde{r}}, k_2)\underline{b}_{mn}(\underline{\tilde{r}}') + \underline{n}_{mn}^{(1)}(\underline{\tilde{r}}, k_2)\underline{b}'_{mn}(\underline{\tilde{r}}')\right), \\ &+ \left(\underline{m}_{mn}^{(2)}(\underline{\tilde{r}}, k_2)\underline{c}_{mn}(\underline{\tilde{r}}') + \underline{n}_{mn}^{(2)}(\underline{\tilde{r}}, k_2)\underline{c}'_{mn}(\underline{\tilde{r}}')\right)\Big], \\ &a_1 \le \tilde{r} \le a_2\end{aligned} \tag{4}$$

where $k_i = k_0\sqrt{\varepsilon_i},\ \underline{a}_{mn}(\underline{\tilde{r}}'),\ \underline{a}'_{mn}(\underline{\tilde{r}}'),\ \ldots,\ \underline{c}'_{mn}(\underline{\tilde{r}}')$ are unknown coefficients to be determined and $\underline{m}_{mn}^{(j)}(\underline{\tilde{r}}, k_i),\ \underline{n}_{mn}^{(j)}(\underline{\tilde{r}}, k_i),\ i = 1, 2;\ j = 1, 2$ are the well known spherical wave functions [11].

Regarding, the region outside the head and inside the ellipsoidal cavity, the electric field $\overline{\underline{G}}_3(\underline{\tilde{r}}, \underline{\tilde{r}}')$ consists of the primary excitation $\overline{\underline{G}}_0(\underline{\tilde{r}}, \underline{\tilde{r}}')$ from the unit source located at $\underline{\tilde{r}}'$ and the contribution of the field $\overline{\underline{G}}_s(\underline{\tilde{r}}, \underline{\tilde{r}}')$, scattered from the double layered sphere. Thus,

$$\overline{\underline{G}}_3(\underline{\tilde{r}}, \underline{\tilde{r}}') = \overline{\underline{G}}_0(\underline{\tilde{r}}, \underline{\tilde{r}}') + \overline{\underline{G}}_s(\underline{\tilde{r}}, \underline{\tilde{r}}') \tag{5}$$

where, $\overline{\underline{G}}_0(\underline{\tilde{r}}, \underline{\tilde{r}}')$ is the free space dyadic Green's function and is defined by an infinite sum of spherical waves as [11, 12].

$$\begin{aligned}\overline{\underline{G}}_0(\underline{\tilde{r}}, \underline{\tilde{r}}') = &\sum_{n=1}^{\infty}\sum_{m=-n}^{n}(-1)^m\frac{-jk_0}{4\pi}\frac{2n+1}{n(n+1)} \\ &\times\begin{cases}\underline{m}_{-mn}^{(1)}(\underline{\tilde{r}}, k_0)\underline{m}_{mn}^{(3)}(\underline{\tilde{r}}', k_0) + \underline{n}_{-mn}^{(1)}(\underline{\tilde{r}}, k_0)\underline{n}_{mn}^{(3)}(\underline{\tilde{r}}', k_0), & \tilde{r} > \tilde{r}' \\ \underline{m}_{-mn}^{(3)}(\underline{\tilde{r}}, k_0)\underline{m}_{mn}^{(1)}(\underline{\tilde{r}}', k_0) + \underline{n}_{-mn}^{(3)}(\underline{\tilde{r}}, k_0)\underline{n}_{mn}^{(1)}(\underline{\tilde{r}}', k_0), & \tilde{r} < \tilde{r}'\end{cases}\end{aligned} \tag{6}$$

(The case $\underline{\tilde{r}} = \underline{\tilde{r}}'$ of Eq. (6) does not appear in the analysis).
while the scattered field mentioned above, given the presence of the closed ellipsoidal cavity, is expressed by

$$\overline{\underline{G}}_s(\underline{\tilde{r}}, \underline{\tilde{r}}') = \sum_{n=1}^{\infty}\sum_{m=-n}^{n}\left[\left(\underline{m}_{mn}^{(1)}(\underline{\tilde{r}}, k_2)\underline{d}_{mn}(\underline{\tilde{r}}') + \underline{n}_{mn}^{(1)}(\underline{\tilde{r}}, k_2)\underline{d}'_{mn}(\underline{\tilde{r}}')\right)\right.$$

$$+\left(\underline{m}^{(2)}_{mn}(\underline{\tilde{r}},k_2)\underline{e}_{mn}(\underline{\tilde{r}}')+\underline{n}^{(2)}_{mn}(\underline{\tilde{r}},k_2)\underline{e}'_{mn}(\underline{\tilde{r}}')\right)\Big],\ \tilde{r}\geq a_2 \tag{7}$$

Hereupon, the unknown expansion coefficients of the infinite sum of spherical waves are determined by the boundary conditions on the interfaces $\tilde{r} = a_1, a_2$ [10–12] and on the conductive surface of the ellipsoidal.

In order to satisfy the continuity of the tangential electric and magnetic field components, the boundary conditions on the interfaces $\tilde{r} = a_1, a_2$ are then imposed by implementing the expressions:

$$\hat{\tilde{r}}\times\overline{\underline{G}}_i(\underline{\tilde{r}},\underline{\tilde{r}}') = \hat{\tilde{r}}\times\overline{\underline{G}}_{i+1}(\underline{\tilde{r}},\underline{\tilde{r}}'),\quad \tilde{r}=a_i;\quad i=1,2 \tag{8}$$

$$\hat{\tilde{r}}\times\left(\nabla\times\overline{\underline{G}}_i(\underline{\tilde{r}},\underline{\tilde{r}}')\right) = \hat{\tilde{r}}\times\left(\nabla\times\overline{\underline{G}}_{i+1}(\underline{\tilde{r}},\underline{\tilde{r}}')\right),\quad \tilde{r}=a_i;\quad i=1,2 \tag{9}$$

where $\hat{\tilde{r}}$ denotes the unit vector along the radial direction of the local coordinate system (Fig. 1). By implementing the orthogonality properties of the spherical wave functions [11], two independent 4×4 linear sets of equations are obtained for the unknown expansion coefficients stated above. These two independent sets can be solved analytically for the coefficients $\underline{a}_{mn}(\underline{\tilde{r}}')$, $\underline{b}_{mn}(\underline{\tilde{r}}')$, $\underline{c}_{mn}(\underline{\tilde{r}}')$ and $\underline{a}'_{mn}(\underline{\tilde{r}}')$, $\underline{b}'_{mn}(\underline{\tilde{r}}')$, $\underline{c}'_{mn}(\underline{\tilde{r}}')$ respectively.

The remaining boundary conditions to be imposed are on the conductive surface of the ellipsoidal cavity, where the dot product of the electric field with both independent unit tangential vectors $\hat{t}_\phi$, $\hat{t}_\eta$ must be zero. The position vector of an arbitrary point on the surface of the ellipsoid in terms of the central coordinate system is defined by

$$\underline{r} = \hat{x}a\cdot\cos\varphi\cdot\sin\eta + \hat{y}a\cdot\sin\phi\cdot\sin\eta + \hat{z}b\cdot\cos\eta \tag{10}$$

Consequently,

$$\hat{t}_\phi = \frac{d\underline{r}\Big/d\phi}{\left|d\underline{r}\Big/d\phi\right|} = -\hat{x}\sin\phi + \hat{y}\cos\phi = \hat{\phi}, \tag{11}$$

which is expected given that the ellipsoidal is by revolution.

Similarly,

$$\hat{t}_\eta = \frac{d\underline{r}\Big/d\eta}{\left|d\underline{r}\Big/d\eta\right|} = \frac{e\left(\hat{x}\cos\phi+\hat{y}\sin\phi\right)\cdot\cos\eta - \hat{z}\sin\eta}{\sqrt{1+(e^2-1)\cos^2\eta}} \tag{12}$$

where $e = a/b$ is the ellipsoid's eccentricity and ϕ, η, the angles depicted in Fig. 1. The electric field at a point $\underline{r}$ lying in any region $i = 1, 2, 3$ can be expressed as

$$\underline{E}_i(\tilde{\underline{r}}) = -j\omega\mu_0 \overline{\underline{G}}_i(\tilde{\underline{r}}, \tilde{\underline{r}}') \cdot \hat{p} \tag{13}$$

where $\overline{\underline{G}}_i(\tilde{\underline{r}}, \tilde{\underline{r}}')$ is the dyadic Green's function in the corresponding region. $\underline{J}(\tilde{\underline{r}}')$ the current distribution of the source dipole placed at $\tilde{\underline{r}}'$. The quantity $\underline{J}(\tilde{\underline{r}}')$ is defined as

$$\underline{J}(\tilde{\underline{r}}') = \hat{p}\,\delta(\tilde{\underline{r}} - \tilde{\underline{r}}') \tag{14}$$

when the dipole is aligned parallel to orientation $\hat{p}$ and $\delta(\tilde{\underline{r}} - \tilde{\underline{r}}')$ is the well-known delta function.

Taking into account the above, the boundary condition on the ellipsoid's surface is expressed by

$$\left.\begin{aligned} \underline{E}_3(\tilde{\underline{r}}) \cdot \hat{t}_\phi = (\underline{E}_s(\tilde{\underline{r}}) + \underline{E}_o(\underline{r}) \cdot \hat{t}_\phi = 0 \\ \underline{E}_3(\tilde{\underline{r}}) \cdot \hat{t}_\eta = (\underline{E}_s(\tilde{\underline{r}}) + \underline{E}_o(\underline{r}) \cdot \hat{t}_\eta = 0 \end{aligned}\right\} \tag{15}$$

Hence, the resulting system from Eq. (15), to be solved, can be written in the form

$$\begin{aligned} &\sum_{n=1}^{\infty} \sum_{m=-n}^{n} \left[Q_{mn} \left(\underline{d}_{mn}(\tilde{\underline{r}}') \cdot \hat{p} \right) + U_{mn} \left(\underline{d}'_{mn}(\tilde{\underline{r}}') \cdot \hat{p} \right) \right] \\ &= -\sum_{n=1}^{\infty} \sum_{m=-n}^{n} \left[A_{mn} \left(\underline{m}^{(3)}_{-mn}(\tilde{\underline{r}}', k_0) \cdot \hat{p} \right) + B_{mn} \left(\underline{n}^{(3)}_{-mn}(\tilde{\underline{r}}', k_0) \cdot \hat{p} \right) \right. \\ &\quad \left. + \underline{E}_o(\underline{r}, \underline{r}') \cdot \hat{t}_\phi \right] \end{aligned} \tag{16a}$$

$$\begin{aligned} &\sum_{n=1}^{\infty} \sum_{m=-n}^{n} \left[S_{mn} \left(\underline{d}_{mn}(\tilde{\underline{r}}') \cdot \hat{p} \right) + T_{mn} \left(\underline{d}'_{mn}(\tilde{\underline{r}}') \cdot \hat{p} \right) \right] \\ &= -\sum_{n=1}^{\infty} \sum_{m=-n}^{n} \left[C_{mn} \left(\underline{m}^{(3)}_{-mn}(\tilde{\underline{r}}', k_0) \cdot \hat{p} \right) + D_{mn} \left(\underline{n}^{(3)}_{-mn}(\tilde{\underline{r}}', k_0) \cdot \hat{p} \right) \right. \\ &\quad \left. + \underline{E}_o(\underline{r}, \underline{r}') \cdot \hat{t}_\eta \right] \end{aligned} \tag{16b}$$

where Q_{mn}, U_{mn}, A_{mn}, B_{mn}, S_{mn}, T_{mn}, C_{mn}, D_{mn} are known scalar coefficients. In Eq. (16a) and Eq. (16b), for the sake of simplicity, instead of implementing the infinite sum of Eq. (6), the vector of the free space field generated by the dipole of effective length l_{eff} and feeding current $I(0) = I_o$ is expressed in Cartesian coordinates by

$$\underline{E}_o(\underline{r}, \underline{r}') = \hat{p}\,(-j\omega\mu_0 I_o l_{eff}) \cdot \left(\overline{\underline{I}} + k_0^{-2} \nabla\nabla \right) \cdot \frac{\exp\left(-jk_0 \left|\underline{r} - \underline{r}'\right|\right)}{4\pi \left|\underline{r} - \underline{r}'\right|}$$

where it is considered $I_o l_{eff} = 1$, $\overline{\underline{I}}$ is the unit dyad and $\hat{p} = \hat{x},\ \hat{y}$ or $\hat{z}$ the dipole's orientation. Once $\underline{d}_{mn}(\tilde{\underline{r}}')$ and $\underline{d}'_{mn}(\tilde{\underline{r}}')$ are computed and consequently, $\underline{a}_{mn}(\tilde{\underline{r}}')$, $\underline{b}_{mn}(\tilde{\underline{r}}')$, $\underline{c}_{mn}(\tilde{\underline{r}}')$, $\underline{e}_{mn}(\tilde{\underline{r}}')$ and $\underline{a}'_{mn}(\tilde{\underline{r}}')$, $\underline{b}'_{mn}(\tilde{\underline{r}}')$, $\underline{c}'_{mn}(\tilde{\underline{r}}')$, $\underline{e}'_{mn}(\tilde{\underline{r}}')$ respectively, it is evident that the electric field can be calculated at any point inside the ellipsoidal cavity and of course, inside and outside the human head model, with very low computational cost.

3. NUMERICAL RESULTS AND VALIDATION OF THE METHOD

The estimation of the electric field, as obtained from the equations of Section 2, consists in the computation of a double sum with respect to the integers n and m, representing the orders of the spherical wave vectors used to express the field at any point inside the ellipsoidal. The infinite sum with respect to n is convergent and, hence, it can be truncated to a finite one. Therefore, Eq. (16) was applied on a mesh of $N(N+2)$ collocation points on the surface of the ellipsoidal by revolution and given the number of terms N required for the convergence, can be equivalently written as

$$\begin{aligned}
&\sum_{n=1}^{N}\sum_{m=-n}^{n}\left[Q_{mn}^{(\tilde{\eta},\tilde{\varphi})}\left(\underline{d}_{mn}(\tilde{\underline{r}}')\cdot\hat{p}\right)+U_{mn}^{(\tilde{\eta},\tilde{\varphi})}\left(\underline{d}'_{mn}(\tilde{\underline{r}}')\cdot\hat{p}\right)\right]\\
&=-\sum_{n=1}^{N}\sum_{m=-n}^{n}\left[A_{mn}^{(\tilde{\eta},\tilde{\varphi})}\left(\underline{m}_{-mn}^{(3)}(\tilde{\underline{r}}',k_0)\cdot\hat{p}\right)+B_{mn}^{(\tilde{\eta},\tilde{\varphi})}\left(\underline{n}_{-mn}^{(3)}(\tilde{\underline{r}}',k_0)\cdot\hat{p}\right)\right.\\
&\left.+\underline{E}_o(\underline{r},\underline{r}')\cdot\hat{t}_{\phi}\right] \qquad (16c)\\
&\sum_{n=1}^{N}\sum_{m=-n}^{n}\left[S_{mn}^{(\tilde{\eta},\tilde{\varphi})}\left(\underline{d}_{mn}(\tilde{\underline{r}}')\cdot\hat{p}\right)+T_{mn}^{(\tilde{\eta},\tilde{\varphi})}\left(\underline{d}'_{mn}(\tilde{\underline{r}}')\cdot\hat{p}\right)\right]\\
&=-\sum_{n=1}^{N}\sum_{m=-n}^{n}\left[C_{mn}^{(\tilde{\eta},\tilde{\varphi})}\left(\underline{m}_{-mn}^{(3)}(\tilde{\underline{r}}',k_0)\cdot\hat{p}\right)+D_{mn}^{(\tilde{\eta},\tilde{\varphi})}\left(\underline{n}_{-mn}^{(3)}(\tilde{\underline{r}}',k_0)\cdot\hat{p}\right)\right.\\
&\left.+\underline{E}_o(\underline{r},\underline{r}')\cdot\hat{t}_{\eta}\right] \qquad (16d)
\end{aligned}$$

The detailed expressions of the scalar coefficients $Q_{mn}^{(\tilde{\eta},\tilde{\varphi})}$, $U_{mn}^{(\tilde{\eta},\tilde{\varphi})}$, $A_{mn}^{(\tilde{\eta},\tilde{\varphi})}$, $B_{mn}^{(\tilde{\eta},\tilde{\varphi})}$, $S_{mn}^{(\tilde{\eta},\tilde{\varphi})}$, $T_{mn}^{(\tilde{\eta},\tilde{\varphi})}$, $C_{mn}^{(\tilde{\eta},\tilde{\varphi})}$, $D_{mn}^{(\tilde{\eta},\tilde{\varphi})}$ in (16c) and (16d) are given in the Appendix A.

The position of each collocation point is determined by the angles $(\tilde{\eta},\tilde{\varphi})$, appearing as indexes in the above equations and in conjunction

with Eq. (2) and (10), are defined as:

$$\tilde{\phi} = \tan^{-1}\left(\frac{\tilde{y}}{\tilde{x}}\right) = \tan^{-1}\left(\frac{a\sin\phi\sin\eta - \delta y}{a\cos\phi\sin\eta - \delta x}\right) \tag{17}$$

$$\begin{aligned}\tilde{\eta} &= \tan^{-1}\left(\frac{\sqrt{\tilde{x}^2 - \tilde{y}^2}}{\tilde{z}}\right) \\ &= \tan^{-1}\left(\frac{\sqrt{(a\cos\phi\sin\eta - \delta x)^2 + (a\sin\phi\sin\eta - \delta y)^2}}{b\cos\eta - \delta z}\right)\end{aligned} \tag{18}$$

where η, φ are the corresponding angles expressed referring to the central coordinate system. The mesh of the collocation points comprises an even number of M cycles parallel to the xy plane with z_i coordinate along the z-axis of the central coordinate system, each one enumerating μ_i points and expressed as:

$$z_i = +b - \frac{2b}{M}(i-1), \quad i = 1, 2, \ldots, M+1 \tag{19}$$

$$\mu_i = \begin{cases} 1, & i = 1, i = M+1 \\ 2^i, & 2 \le i < \dfrac{M}{2} \\ 2^{M/2}, & i = \dfrac{M}{2} \\ 2^{M-(i-2)}, & \dfrac{M}{2} < i \le M \end{cases} \tag{20}$$

At this point, the magnitude of the angles η_i, φ_i of an arbitrary point on the surface of the ellipsoid (Fig. 1), is expressed as a function of z_i and μ_i as

$$\eta_i = \tan^{-1}\left(\frac{R_i}{z_i}\right), \tag{21}$$

where $R_i = a\left(1 - \left(\frac{z_i}{b}\right)^2\right)^{1/2}$, a, b are the dimensions of the ellipsoid and

$$\varphi_i = \begin{cases} 0, & j = 1,\ j = M+1 \\ \dfrac{2\pi}{\mu_i}(j-1), & j = 1, \ldots, \mu_i + 1 \end{cases} \tag{22}$$

The number of the collocation points emerging from this procedure is equal to $2^{\frac{M}{2}+2} - 6$. As stated above though, the total number

of collocation points required is $N(N+2)$ and hence, the remaining collocation points are: $X = N(N+2) - \left(2^{\frac{M}{2}+2} - 6\right)$ and are placed on the major circle (with radius $r = b$) of the transversal section of the ellipsoid. By observing Eq. (19) it is evident that the cycle in question is not included. Therefore, the characteristic values of the angles η, φ_j for this case are:

$$\eta = \frac{\pi}{2} \text{ and } \phi_j = \frac{2\pi}{X}(j-1),\ j = 1, \ldots, X+1 \tag{23}$$

Thus, by determining the position of every collocation point via the calculated values of Eq. (21)–(23), the values of the angles $\tilde{\eta}$, $\tilde{\varphi}$ appearing in the $(2N(N+2)\times 2N(N+2))$ system to be solved (Eq. (16c) and (16d)), are obtained from expressions (17) and (18).

The problem was solved for two different frequencies $f_1 = 1.5\,\text{GHz}$ and $f_2 = 3.5\,\text{GHz}$. The dimensions of the ellipsoid used for the computation, which were the actual dimensions of the constructed cavity, were $a = 60\,\text{cm}$, $b = 75\,\text{cm}$ with inter-focal distance $2c = 2\sqrt{b^2 - a^2} = 90\,\text{cm}$.

The dielectric properties of the tissue composition used for the computation are $\varepsilon_1 = 50.74$, $\sigma_1 = 1.23$ for brain (gray matter) and $\varepsilon_2 = 8.0$, $\sigma_2 = 0.14$ for skull at 1.5 GHz [13, 14]. The respective values for the frequency of 3.5 GHz are: $\varepsilon_1 = 47.31$, $\sigma_1 = 2.64$ for brain (gray matter) and $\varepsilon_2 = 7.9$, $\sigma_2 = 0.25$ for skull [13, 14]. The magnetic properties of the layers are denoted as $\mu_1 = \mu_2 = \mu_0$. The head model, including skull (6–8 mm of thickness) and thick brain (gray matter) is of total diameter 15 cm [15] and hence, $a_1 = 6.8\,\text{cm}$ and $a_2 = 7.5\,\text{cm}$.

The size of the spherical object, its electrical characteristics and especially the ratio of the sphere's radius to the ellipsoid's major axis, affect critically the number of the terms required for the infinite sum to converge. For the cases treated in this paper, it has been observed that truncation of the infinite sum with respect to the order n of the spherical wave vectors in the order of $N = 11$ and $N = 17$ for the 1.5 GHz and 3.5 GHz frequency respectively, ensures convergence of the obtained solution at any point. The predictions of the Green's function code for the magnitude of the electric field for two successive runs of the convergent number of terms show satisfying agreement (in the order of 2%–3%). The continuity of the tangential fields at the $\tilde{r} = a_1,\ a_2$ interface planes between different layers has been checked and verified numerically (excellent agreement in the order of 2‰–3‰), while the validity of the boundary conditions on the surface of the ellipsoidal has also been checked. Finally, comparison of the results using the proposed semi-analytical technique with results obtained by a software package for electromagnetic modeling of passive, three-

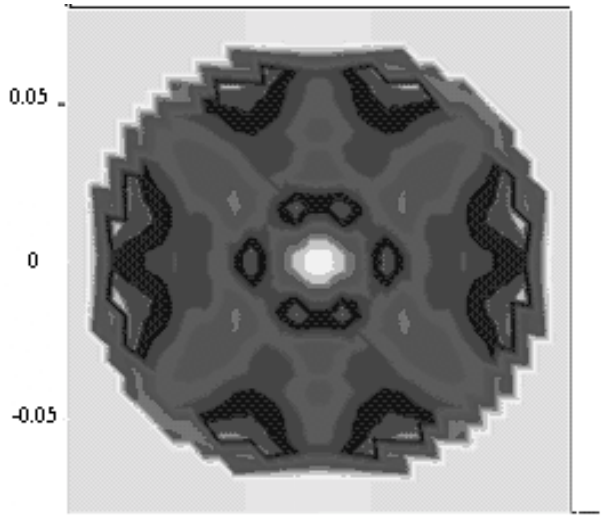

Figure 2. XY cut plane of the head model at the focal point at 1.5 GHz.

dimensional structures (High-Frequency Structure Simulator, HFSS [16]), has shown completely equivalent results.

The results of the computation are depicted in the Figs. 2, 3 and 4 where the plots of the magnitude of the electric field in transversal sections of the head model when its center is placed on the focal point and the source dipole is of z-orientation, are shown. Clear focusing of the electric field inside the human head model can be observed. In the case of the 1.5 GHz operation frequency, the penetration depth is in the order of more than 3 cm (Fig. 2) while in the case of the 3.5 GHz frequency, it doesn't exceed 2 cm of depth (Fig. 4). The maximum values of the electric field distribution inside the head model are represented by the darkest shaded areas in the relevant figures. By comparing the XY plane cut depicted in Fig. 3 which is 2.5 cm away from the focus plane, with the corresponding figure to the XY focus (Fig. 2) cut, it is evident that the electric field clearly merges on the focus where the center of the human head model is placed. In Fig. 5 and 6 the respective results obtained by HFSS are depicted and are in excellent agreement with those resulting from the code.

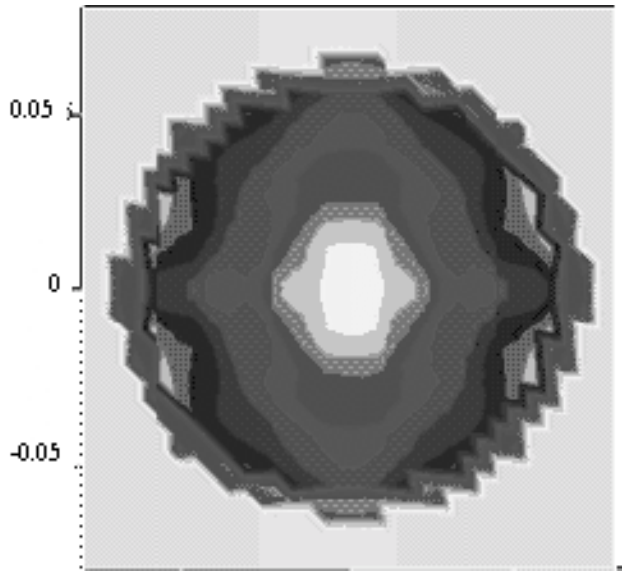

Figure 3. XY cut plane of the head model moved 2.5 cm along z-axis at 1.5 GHz.

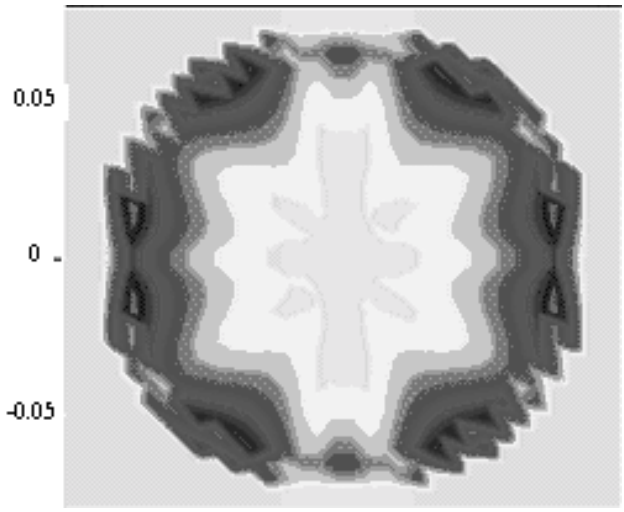

Figure 4. XY cut plane of the head model at the focal point at 3.5 GHz.

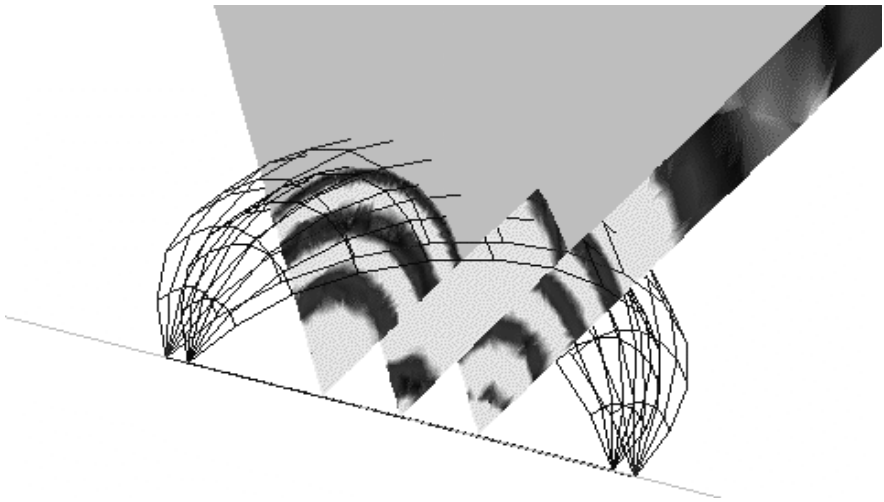

Figure 5. *XY* cut planes of the head model at the focal point and at ± 2.5 cm away at 1.5 GHz.

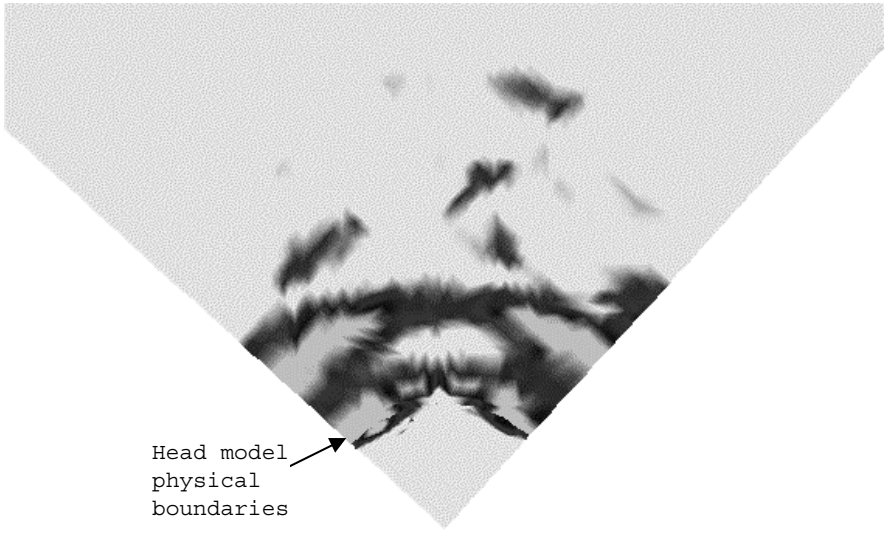

Figure 6. *XY* cut planes of the head model at the focal point at 3.5 GHz.

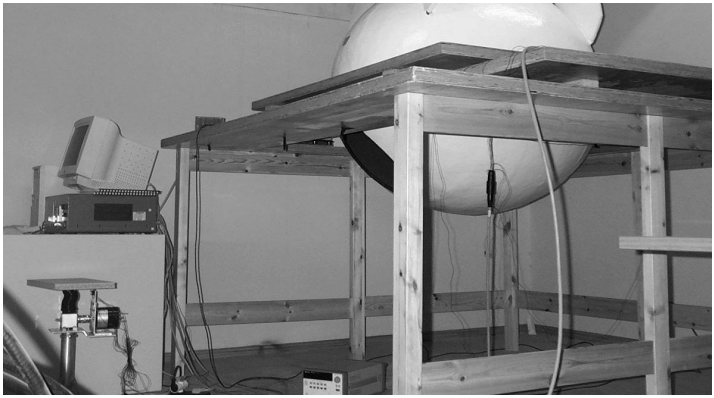

Figure 7. Experimental set-up — The microwave radiometry device.

4. EXPERIMENTAL PROCEDURE AND RESULTS

4.1. Experimental Set-up

The 3D microwave radiometric imaging device that was designed and constructed in the framework of the present research is shown in Fig. 7. It consists of an ellipsoidal conductive wall cavity, a radiometric receiver operating at 3.5 GHz, and a relevant non-contact receiving antenna. The characteristic property of the ellipsoidal [17] is that every ray originating from one focal point will converge to the other focal point with the same path length. Hence, all the rays of the radiated energy of a source starting from one focus converge to the other by keeping their total path lengths equal, following a single reflection inside the conductive wall cavity. The inner surface of the cavity is painted with a conducting paint to achieve a good reflection of incident electromagnetic waves.

The total power radiometer was designed and constructed using microstrip line technology, with frequency characteristics of (F_c = 3.5 GHz, BW = 200 MHz, Noise Figure = 1.23 dB). The use of chip devices, which dissipate power varying with temperature, fact that results in temperature compensation and replace closed loop temperature compensation circuits to limit gain drift, is foreseen.

A standard sleeve cross-dipole was constructed using a semi-rigid coaxial line. The antenna was positioned in parallel to the ellipsoid's major axis, in order to receive all the reflected waves on the walls of the conductive cavity, in other words all polarizations.

The signal incident on the antenna is amplified and filtered sequentially and then fed to an integrator-low pass filter and driven to

a dc amplifier. The measured voltage at the output of the radiometer is proportional to [18]

$$I \cong (\omega_0^2 \mu_0 k/\pi) \cdot \Delta\omega \cdot c_t \cdot T(\underline{r}_A) \cdot \sigma(\underline{r}_A) \tag{24}$$

where, ω_0 is the center frequency (in radians/sec) of the observed microwave spectrum bandwidth, μ_0 is the magnetic permeability constant, $\Delta\omega$ is the bandwidth of the observed microwave spectrum, c_t the speed of light in free space, $T(\underline{r}_A)$ is the temperature spatial distribution within the medium of interest, and $\sigma(\underline{r}_A)$ is the spatial distribution within the medium of interest for the electric conductivity. Therefore, the measured output voltage is correlated linearly to the product of $T(\underline{r}_A)\sigma(\underline{r}_A)$ of the subject under measurement. In the case of the water phantom experiments where there is variation of temperature while the conductivity remains unchanged, it is evident that the measured voltage provides estimations of temperature.

The base band signal at the output of the dc amplifier is sent to an A/D acquisition card, which processes the measurement data. The imaging system's movement and data acquisition (sampling and averaging) is controlled by a PC which is programmed to permit a three dimensional movement of the system and therefore various measurement modes: single selected points, surface (two dimensional) and volume scans (three dimensional). This way, the system's temperature and spatial resolution can be accurately defined. With a view to verify the proof of concept and estimate the system's temperature and spatial resolution, experiments using a small thermo-insulating water phantom, were performed.

4.2. Temperature Resolution

A small cube (5 cm × 5 cm × 5 cm) made of thermal insulating material with a small opening of (2 cm × 2 cm × 2 cm) containing a quantity of water of several ml at different temperatures with its center placed at the focal point, was used for this experiment. The thermal insulating material ensures the minimization of thermal dissipation and cooling of the content of the phantom. The phantom was chosen to have small dimensions in order to verify the prediction of the 3 db volume of the focal region, obtained from the numerical results and in order to provide homogeneity of temperature distribution of the water it contains. As reported above the measured voltage is linearly correlated to the product of the subject under measurement. In this case, the conductivity of the water phantom remains stable and therefore the system's output curves provide voltage and temperature correlations. In Fig. 8 the expected linearity of the system is

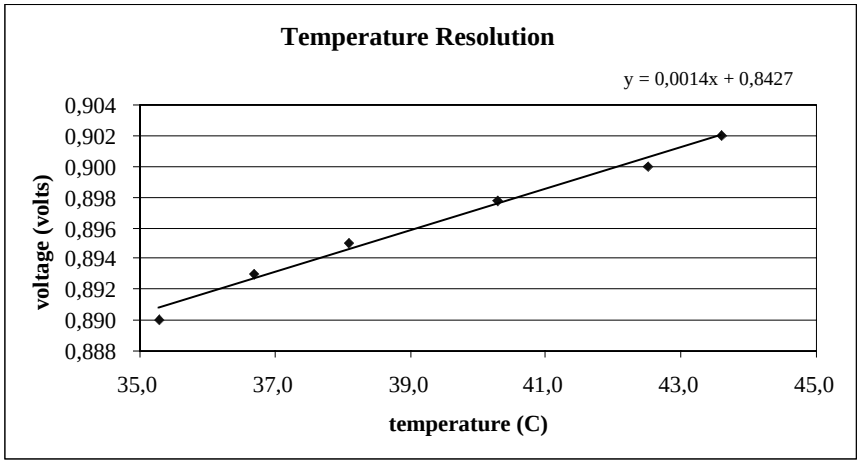

Figure 8. Output voltage versus temperature of water phantom.

observed. The phantom was filled each time with water at different temperatures in the range of 35°C–45°C, which was measured with a precision centigrade temperature sensor. During a time interval of 8 seconds, 8000 samples were obtained for each measured point (output voltage for each measured water temperature) with sampling rate 1000 samples/sec. After the averaging procedure, the results of the measured output voltage corresponding to the relevant water temperature of the phantom are depicted in Fig. 8. The temperature accuracy of the system is in the order of (1.5 ± 0.5) mV/°C and in terms of temperature is approximately 1°C. Finally, with this measurement the capability of the system to detect small concentrated sources is verified. Throughout the experiment the background voltage, which was obtained with data acquisition of the response of an empty cavity (no phantom present), was (0.5175 ± 0.0005) Volts.

4.3. Spatial Resolution

In order to estimate the spatial accuracy of the device, linear displacements from the focal point with small increment steps of the same water phantom were realized. During a time interval of 8 seconds, 8000 samples were obtained for each measured point (water of certain temperature at each displacement position) with sampling rate 1000 samples/sec. Initially, the water phantom was filled with water of 38°C. The device was programmed to make the following movement: initially, 10 measurements were obtained with the phantom

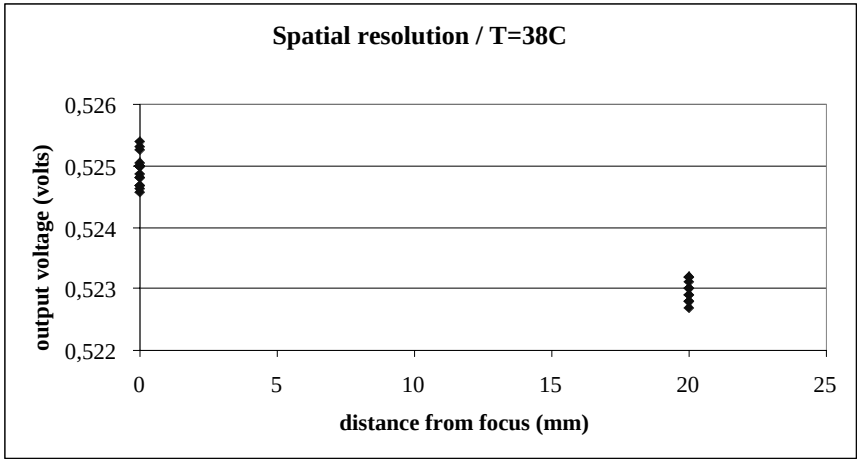

Figure 9. Output voltage of water phantom at 38°C at the focal point and 2 cm away from the focus.

placed on the focal point with the sampling rate stated above, followed by the acquisition of the output voltage during the displacement of the focal point of 2 cm along the Y-axis. Continuing, 5 measurements were obtained at each one of the mentioned positions. The experiment ended with the acquisition of 10 more values of the device's output voltage with the center of the small container placed on the focal point. In Fig. 9 it is observed that the voltage drops 2 mV when the phantom is moved away from the focus as much as 2 cm, with a measurement voltage accuracy of 0.0005 V. Linear scans along each one of the three orthogonal axes, show similar results.

The next experiment aimed at determining accurately the system's spatial resolution, therefore smaller increment steps of 0.5 cm were implemented. The water's temperature was 0.5 C less than the first experiment (37.5 C), fact that explains the reduction of the detected signal when the phantom is at the focal point. The same experimental procedure was adopted. The results are depicted in Fig. 10 where it is evident that the system is able of detecting sources which are at least 1cm apart. Safe conclusions about the positions of sources that are placed 5 mm away from each other can not be obtained, as shown on the graph.

Finally, in order to verify the system's spatial accuracy of 1 cm for weaker sources, the same phantom was filled with water of 36 C and the former experiment was repeated. With this configuration the temperature and spatial accuracy of the device can be validated at

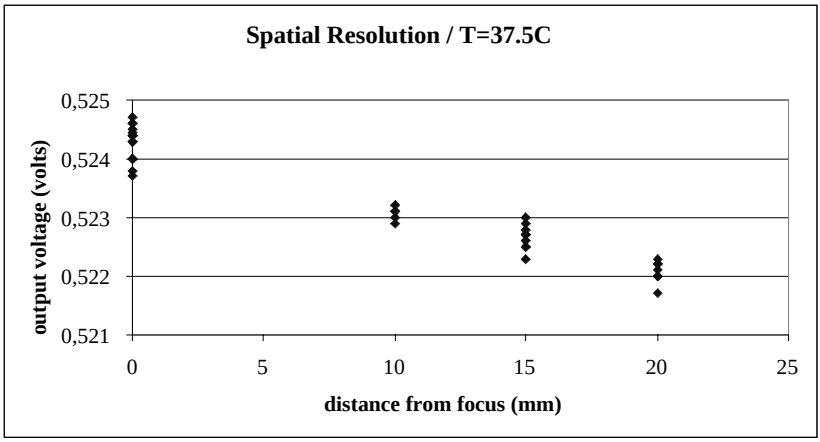

Figure 10. Output voltage of water phantom at 37.5°C at the focal point and 1, 1.5 and 2 cm away from the focus.

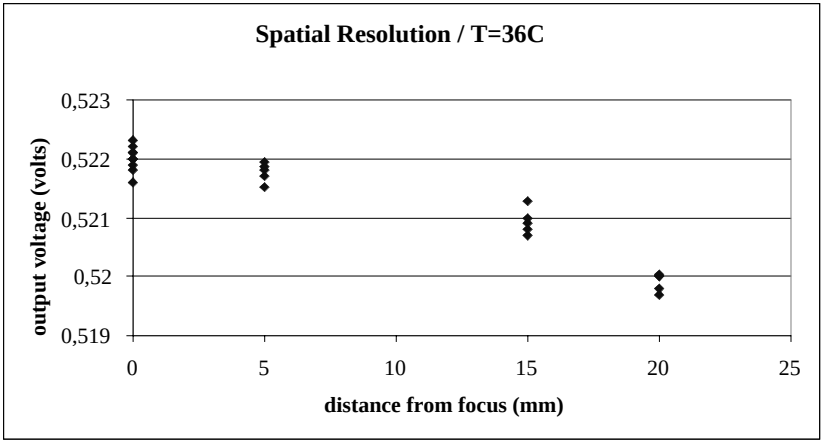

Figure 11. Output voltage of water phantom at 36°C at the focal point and 0.5, 1.5 and 2 cm away from the focus.

the same time: the reduction of the detected signal will lead to a reassessment of the temperature resolution and the spatial resolution will be verified with the comparison of the measured output voltage for the same increment steps of displacement from the focal region. The results are shown in Fig. 11. Indeed, in this case the measured voltage when the phantom placed at the focus is 3 mV less than the respective value of the first experiment. According to the system's temperature

resolution obtained from experiments in Section 4.1, this corresponds to 2°C of temperature difference, fact that is valid. Also, it is observed that for every 1 cm step the output voltage is reduced as much as 1 mV which is in complete accordance with the results obtained from the former experiment.

5. DISCUSSION AND CONCLUSIONS

In this paper, a semi-analytical technique has been presented for the study of the estimation of the electric field inside an ellipsoidal cavity, generated by a dipole positioned on one focal point with the presence of a double layered model of the human head, placed on the other focus of the elliptical reflector. The proposed method is based on a Green's function methodology. Validation checks of the method have been performed in comparison with the results obtained from a simulator for two operating frequencies, 1.5 GHz and 3.5 GHz. According to the theoretical analysis using the human head model, both Green's function theory and simulations predicted to obtain a penetration depth of more than 4 cm and less than 2 cm at 1.5 GHz and 3.5 GHz respectively. The radius of the focal region where maximum electric filed is observed is approximately 3 cm and 1.5 cm at 1.5 GHz and 3.5 GHz correspondingly.

The system described in the electromagnetic analysis was designed and constructed for future possible intracranial applications. Experiments were performed in order to evaluate the prototype non-invasive radiometric imaging system that consists of a conducting wall ellipsoidal cavity with a microwave radiometric system as receiver, operating at 3.5 GHz. The temperature sensitivity of the system according to the phantom experiments is estimated approximately 1°C. Based on the experimental analysis, with phantoms, the system's spatial resolution is 1 cm.

Referring to the systems feasibility in possible clinical and medical applications, the device may be used in cases when the temperature variations are in the order of at least 1°C, such as temperature monitoring in hyperthermia sessions, heat strokes or meningioma in the brain where significant temperature changes take place. The system is estimated from the theoretical analysis to provide high spatial resolution ability in presence of the human head despite the mismatch between air and head interface. In order to achieve various penetration depths inside subcutaneous tissues and variant spatial accuracy of the system depending on the focusing properties of the system at different frequency ranges, radiometric receivers operating at various frequencies or multi-band receivers provide results in this direction.

APPENDIX A.

The scalar coefficients appearing in equations (16c) and (16d) are expressed as follows:

$$Q_{mn}^{(\tilde{\eta},\tilde{\varphi})} = \underline{m}_{mn}^{(1)}(\underline{\tilde{r}}_c, k_0)\cdot\hat{\phi} - \frac{D_n}{E_n}\underline{m}_{mn}^{(2)}(\underline{\tilde{r}}_c, k_0)\cdot\hat{\phi} \tag{A1}$$

$$U_{mn}^{(\tilde{\eta},\tilde{\varphi})} = \underline{n}_{mn}^{(1)}(\underline{\tilde{r}}_c, k_0)\cdot\hat{\phi} - \frac{D'_n}{E'_n}\underline{n}_{mn}^{(2)}(\underline{\tilde{r}}_c, k_0)\cdot\hat{\phi} \tag{A2}$$

$$S_{mn}^{(\tilde{\eta},\tilde{\varphi})} = \underline{m}_{mn}^{(1)}(\underline{\tilde{r}}_c, k_0)\cdot\hat{t}_\eta - \frac{D_n}{E_n}\underline{m}_{mn}^{(2)}(\underline{\tilde{r}}_c, k_0)\cdot\hat{t}_\eta \tag{A3}$$

$$T_{mn}^{(\tilde{\eta},\tilde{\varphi})} = \underline{n}_{mn}^{(1)}(\underline{\tilde{r}}_c, k_0)\cdot\hat{t}_\eta - \frac{D'_n}{E'_n}\underline{n}_{mn}^{(2)}(\underline{\tilde{r}}_c, k_0)\cdot\hat{t}_\eta \tag{A4}$$

where $\underline{\tilde{r}}_c$ is the position vector of a given collocation point, expressed according to the local coordinate system discussed above.

$$\begin{aligned} D_n &= \Big\{\Big(j_n(k_2a_2)j_n^d(k_0a_2) - j_n^d(k_2a_2)j_n(k_0a_2)\Big) \\ &\quad + \zeta_{mn}\Big(y_n(k_2a_2)j_n^d(k_0a_2) - y_n^d(k_2a_2)j_n(k_0a_2)\Big)\Big\} \end{aligned} \tag{A5}$$

$$\begin{aligned} E_n &= -\Big\{\Big(j_n^d(k_2a_2)y_n(k_0a_2) - j_n(k_2a_2)y_n^d(k_0a_2)\Big) \\ &\quad + \zeta_{mn}\Big(y_n^d(k_2a_2)y_n(k_0a_2) - y_n(k_2a_2)y_n^d(k_0a_2)\Big)\Big\} \end{aligned} \tag{A6}$$

$$\begin{aligned} D'_n &= \Big\{\Big(k_0^2 j_n^d(k_2a_2)j_n(k_0a_2) - k_2^2 j_n(k_2a_2)j_n^d(k_0a_2)\Big) \\ &\quad + \zeta'_{mn}\Big(k_0^2 y_n^d(k_2a_2)j_n(k_0a_2) - k_2^2 y_n(k_2a_2)j_n^d(k_0a_2)\Big)\Big\} \end{aligned} \tag{A7}$$

$$\begin{aligned} E'_n &= -\Big\{\Big(k_2^2 j_n(k_2a_2)y_n^d(k_0a_2) - k_0^2 j_n^d(k_2a_2)y_n(k_0a_2)\Big) \\ &\quad + \zeta'_{mn}\Big(k_2^2 y_n(k_2a_2)y_n^d(k_0a_2) - k_0^2 y_n^d(k_2a_2)y_n(k_0a_2)\Big)\Big\} \end{aligned} \tag{A8}$$

where j_n, y_n are the spherical Bessel and Neumann functions respectively and $z_n^d(x) = \Big(d[xz_n(x)]\Big/dx\Big)$, with z_n being either of the j_n, y_n functions and $\underline{c}_{mn}(\underline{\tilde{r}}') = \zeta_{mn}\underline{b}_{mn}(\underline{\tilde{r}}')$, $\underline{c}'_{mn}(\underline{\tilde{r}}') = \zeta'_{mn}\underline{b}'_{mn}(\underline{\tilde{r}}')$.

Continuing,

$$A_{mn}^{(\tilde{\eta},\tilde{\varphi})} = -E_{mn}\frac{D_n}{E_n}\underline{m}_{mn}^{(2)}(\underline{\tilde{r}}_c, k_0)\cdot\hat{\phi} \tag{A9}$$

$$B_{mn}^{(\tilde{\eta},\tilde{\varphi})} = -E_{mn}\frac{D'_n}{E'_n}\underline{n}_{mn}^{(2)}(\underline{\tilde{r}}_c, k_0)\cdot\hat{\phi} \tag{A10}$$

where, $E_{mn} = (-1)^m \frac{-jk_0}{4\pi}\frac{2n+1}{n(n+1)}(-j\omega\mu_0)$.

Similarly,

$$C_{mn}^{(\tilde{\eta},\tilde{\varphi})} = -E_{mn}\frac{D_n}{E_n}\underline{m}_{mn}^{(2)}(\tilde{\underline{r}}_c, k_0)\cdot\hat{t}_\eta \tag{A11}$$

$$D_{mn}^{(\tilde{\eta},\tilde{\varphi})} = -E_{mn}\frac{D'_n}{E'_n}\underline{n}_{mn}^{(2)}(\tilde{\underline{r}}_c, k_0)\cdot\hat{t}_\eta \tag{A12}$$

REFERENCES

1. Hand, J. W., G. M. J. Van Leeuwen, S. Mizushina, J. B. Van de Kamer, K. Maruyama, T. Suiura, D. V. Azzopardi, and A. D. Edwards, "Monitoring of deep brain temperature in infants using multi-frequency microwave radiometry and thermal modeling," *Physics in Medicine and Biology,* Vol. 46, No. 6, 1885–1903, 2001.
2. Maruyama, K., S. Mizushina, T. Sugiura, G. M. J. Van Leeuwen, J. W. Hand, G. Marrocco, F. Bardati, A. D. Edwards, D. Azzopardi, and D. Land, "Feasibility of noninvasive measurement of deep brain temperature in newborn infants by multifrequency microwave radiometry," *IEEE Transactions on Microwave Theory and Techniques,* Vol. 48, No. 11, 2141–2147, November 2000.
3. Van Leeuwen, G. M. J., et al., "New temperature retrieval algorithm for brain temperature monitoring using microwave brightness temperatures," *Electronic Letters,* Vol. 36, No. 6, 341–342, 2001.
4. Paglione, R., "Portable diagnostic radiometer," *RCA Review,* Vol. 47, 635–643, 1986.
5. Abdul-Razak, M., B. A. Hardwick, G. L. Hey-Shipton, P. A. Matthews, J. R. Monson, and R. C. Kester, "Microwave thermography for medical applications," *IEE Proceedings,* Vol. 134, A, 171–174, 1987.
6. Dubois, L., J. P. Sozanski, V. Tessier, J. Camart, J. J. Favre, J. Pribetich, and M. Chivé, "Temperature control and thermal dosimetry by microwave radiometry in hyperthermia," *IEEE Transactions on Microwave Theory and Techniques,* Vol. 44, 1755–1761, 1996.
7. Edrich, J. and P. C. Hardee, "Thermography at millimeter wavelength," *Proceedings IEEE,* Vol. 62, 1391–1392, 1974.
8. Michaelson, S. M., "Human exposure to nonionizing radiant energy — Potential hazards and safety standards," *Proceedings IEEE,* Vol. 60, 389–921, Apr. 1972.

9. Planck, M., *Eight Lectures on Theoretical Physics,* Dover Pub. Inc., Mineola, New York 1998 (Translator A. P. Wills, first publication 1909 by Columbia Univ. Press).
10. Cottis, P. G. and N. K Uzunoglu, "Focusing properties of dipole arrays placed near a multilayer lossy sphere," *J. Electromag. Waves Applicat.,* Vol. 4, 431–440, 1990.
11. Morse, P. M. and H. Feshbach, *Methods of Theoretical Physics,* Part II, Ch. 13, McGraw-Hill, New York, 1953.
12. Nikita, K. S., G. S. Stamatakos, N. K. Uzunoglu, and A. Karafotias, "Analysis of the interaction between a layered spherical human head model and a finite-length dipole," *IEEE Transactions on Microwave Theory and Techniques,* Vol. 48, No. 11, 2003–2013, November 2000.
13. Gabriel, S., R. W. Lau, and C. Gabriel, "The dielectric properties of biological tissues: II. Measurements in the frequency range 10 Hz to 20 GHz," *Physics and Medicine and Biology.,* Vol. 41, 2251–2269, 1996.
14. Stuchly, M. A. and S. S. Stuchly, "Dielectric properties of biological substances — Tabulated," *J. Microwave Power,* Vol. 15, 19–26, 1980.
15. Drossos, A., V. Santomaa, and N. Kuster, "The dependence of electromagnetic energy absorption upon human head tissue composition in the frequency range of 300–3000 MHz," *IEEE Transactions on Microwave Theory and Techniques,* Vol. 48, No. 11, 1988–1995, November 2000.
16. www.ansoft.com
17. Heath, Sir Thomas, "Conic Sections," *A History of Greek Mathematics,* Volume II, Chapter XIV, Apollonius of Perga, Dover Pub. Inc., New York, 1981.
18. Cottis, P. G., N. K. Uzunoglu, and P. S. Papakonstantinou, "Measurement of three-dimensional temperature distribution inside dielectric objects using near-field radiometry," *Journal of Electromagnetic Waves and Applications,* Vol. 2, 621–633, 1988.